A vertical-mode extrapolation scheme applied to the Brazil Current domain: quasi-synoptic scenarios

João P. M. Amorim[1]*, Ilson C. A. da Silveira [1], Milton Borges-Silva[1], Pedro W. M. Souza-Neto[1], Wellington C. Belo[2], Cauê Z. Lazaneo [1], Piero S. Bernardo [1], Marcelo Dottori [1], Renato P. Martins [2] and Daniel L. Moreira [2]

[1] Instituto Oceanográfico - Universidade de São Paulo, Praça Oceanográfico, 191 - Vila Universitaria, São Paulo - SP, 05508-120,
[2] Centro de Pesquisas, Desenvolvimento e Inovação Leopoldo Américo Miguez de Mello - CENPES/PETROBRAS, Av. Horácio Macedo, 950 - Cidade Universitária da Universidade Federal do Rio de Janeiro, Rio de Janeiro - RJ, 21941-915
*Corresponding author: jpedroamorim@alumni.usp.br

ABSTRACT

The Brazil Current (BC) is a western boundary current, with an average vertical extension of 500 m, which occupies the southwestern margin of Atlantic Ocean. Recently, the South Brazil Bight - SBB (23°S - 28°S) has been intensively explored by the oil and gas industries, which brought a high demand in operational oceanography and ocean state monitoring. In this study we present a new technique based on the vertical dynamic modes of oscillation, to extrapolate velocity profiles in the SBB, with potential applications to data acquired by Vessel Mounted Acoustic Doppler Current Profilers (VMADCP). Using four quasi-synoptic cross-sectional velocity data, acquired by Lowered Acoustic Doppler Current Profilers (LADCP), we observed that the mean circulation of this region can be characterized as a 2-dynamical mode system. This mean circulation is mainly dominated at surface by the BC and at intermediate levels by the Intermediate Western Boundary Current (IWBC), which flows northward. Furthermore, observed mesoscale vortical features in the SBB, such as eddies and meanders, are shown to be primarily barotropic-mode dominated. In our extrapolation methodology, the use of an independent set of velocity time series obtained by four moorings has shown to be a valid way for obtaining the relative contribution of each dynamical mode in the velocity field in the SBB. Normalized mean squared errors below 10% and radar diagrams show that the presented methodology was able to reproduce the main dynamic features observed by LADCP transects. Also, with this technique, we extrapolated three VMADCP sections and the results agreed with previous observations.

Keywords: Brazil Current System; Quasi-Synoptic sections; Modal Extrapolation; Dynamical Extrapolation; Operational Oceanography.

INTRODUCTION

The Brazil Current (BC) is a western boundary current which occupies the continental margin of the South Atlantic Ocean. This current originates with the arrival and bifurcation of branches of the South Equatorial Current (SEC) and flows southward until it reaches the Brazil-Malvinas confluence region (Gordon 1989, Soutelino et al. 2011, Luko et al. 2021). The BC increases in thickness while flowing through the South Brazil Bight (SBB), located between 23°S and 28°S (Loder et al. 1998).

This thickening south of 28°S is due to the southernmost branch of the SEC which bifurcates at the Santos Bifurcation (SB) (Boebel et al. 1999, Legeais et al. 2013, Luko et al. 2021). At this region, the BC core can typically be observed centered on the isobaths of 800 m to 1400 m, with speeds that exceed 0.5 m s^{-1} (Silveira et al. 2000, Silveira et al. 2004, Rocha et al. 2014). This current transports two water masses between 21°S and 28°S: the Tropical Water (TW) at surface, and the South Atlantic Central Water (SACW) at pycnoclinic levels (Stramma & England 1999). Below the BC, we find the Intermediate Western Boundary Current (IWBC), originated from the northern branch of the SB (Boebel et al. 1999, Luko et al. 2021). This intermediate current has an average thickness of 1000 m, and flows towards the equator, with a transport range similar to that of the BC (Boebel et al. 1999, Silveira et al. 2004, Costa et al. 2017). Due to the IWBC vertical position, its flow is composed of the Antarctic Intermediate Water (AAIW) and the Upper Circumpolar Deep Water (UCDW) (Boebel et al. 1999, Silveira et al. 2004) and its core coincides with the AAIW salinity minimum, between 700 m and 900 m. Typical core speeds of 0.25 m s^{-1} have been observed (Silveira et al. 2004, Silveira et al. 2008, Legeais et al. 2013).

At the SBB, there is the São Paulo Plateau (SPP), a geomorphological feature that alters the continental slope on deep waters regions (> 2500 m) and replaces the continental rise off Southeast Brazil. This plateau was formed as the result of salt deposition approximately 120 million years ago (Meisling et al. 2001, Duarte & Viana 2007). Due the presence of the SPP, the Deep Western Boundary Current (DWBC) is displaced to the abyssal plain. This current transports North Atlantic Deep Water (NADW) poleward along the southeastern continental margin. Therefore, the current system composed of the poleward BC flow and the equatorward IWBC flow resembles a baroclinic jet similar to the first baroclinic mode (Silveira et al. 2008, Rocha et al. 2014, Biló et al. 2014) and occupies the continental slope in the 1500–1800 m range.

In the past 20 years, this area has been a focus of attention of the oil industry due to its sedimentary basins (Campos and Santos basins). The oil-industry investigations have resulted in a growing knowledge of these basins, involving geological approaches and also brought new demands for operational oceanography, indeed there is still a lack of monitoring for the western boundary currents. Biló et al. (2014) was one of the first studies that combined both operational and dynamic oceanography in the Santos Basin to obtain geostrophic velocity estimates using mainly the dynamic method.

Following Biló et al. (2014), in this work, we propose another methodology to estimate quasi-synoptic cross-sectional speeds of the BC-IWBC system within the SBB. While these authors based their methodology on the thermal wind balance, our speeds estimates are based on a dynamical modes approach according to the interpolation firstly proposed by Wunsch (1997) on current-meter time-series data. Therefore, our proposed methodology has potential applications to data acquired by Vessel Mounted Acoustic Doppler Current Profiler (VMADCP) alone or together with Conductivity Temperature and Depth (CTD) casts.

This paper is organized as follows: section 2 describes the data and methods employed in this effort; section 3 describes the modal composition of observed LADCP current profiles. On section 4 we conduct sensitivity tests to the extrapolation method; and on section 5 the modal extrapolation is applied on the VMADCP data collected in the SBB.

DATA AND METHODS

Shipboard Measurements

Four datasets are used in this study. Three are from the CERES campaigns, which consisted of quasi-synoptic hydrographic surveys to investigate the BC and its recirculation cells. The other is from the MR03-K04 cruise (hereafter MR03) during the World Ocean Circulation Experiment (WOCE). In all the cruises, top-bottom current profiling was performed using a 307.2 kHz Teledyne WorkHorse Lowered Acoustic Doppler Current Profiler (LADCP). The average velocity profile at each station was calculated following the procedures described by Fischer & Visbeck (1993) and Visbeck (2002).

The CTD profiles were performed simultaneously with LADCP profiling using a Seabird SBE Sealog-

Table 1. Names and dates of the cruises conducted at SBB analyzed in this study.

Survey name	Dates	Number of stations
CERESIII	2009/05/06 - 2009/05/12	6
CERESIV	2010/06/08 - 2010/06/20	9
CERESV	2013/10/31 - 2013/11/23	8
MR03	2003/11/07 - 2003/11/11	10

ger on the continental slope of the SBB (Figure 1). The downcast data were spike-removed, averaged into a 1 m bin, and smoothed using a 21-point Hanning filter. We use the Gibbs SeaWater (GSW) Oceanographic Toolbox of the Thermodynamic Equation of SeaWater TEOS-10 (McDougall & Barker 2011) to compute the conservative temperature, absolute salinity and neutral density.
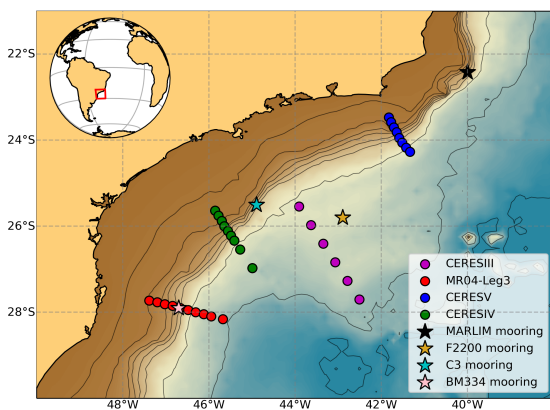
Figure 1. Station map with bathymetry from ETOPO in the background. Colored points represent the LADCP-CTD stations and colored stars the location of the moorings used in this study.

MOORING DATA

In this study, we also use current meter data from a total of four moorings deployed in the SBB during different projects (Table 2). Moored current processing consists of spike-removing and low-pass filter. We rotate the velocity vectors to obtain the along-slope component. We use the mooring data to obtain the average along-slope velocity profiles and use them as representative of the mean circulation. The only exception is the MARLIM mooring, in which we use the average along-slope profile obtained by Silveira et al. (2008).

SATELLITE DATA

Satellite observations are employed using the multi-satellite altimetry Absolute Dynamic Topography (ADT) Level 4 product and derived geostrophic currents produced by the Sea Level Thematic Center (SL-TAC). This product spans from January 1993 to the present and is distributed by Copernicus Marine Environment Monitoring Service (CMEMS, https://www.copernicus.eu/en). A general description of the product can be found on Pujol & Mertz (2019).

WORLD OCEAN ATLAS 2018

The World Ocean Atlas 2018 - WOA2018 (Boyer et al. 2018) is the latest product from a series of oceanographic analyses, which began with the classical work of Levitus (1982), thus continuing more than forty years of efforts to calculate oceanic properties and their distribution in global atlases. WOA2018 consists of a set of climatological data obtained through objective analysis of *in situ* measurements for variables such as temperature, salinity, oxygen, phosphate, among others. In this study, we use the WOA2018 to obtain climatological buoyancy frequency profiles.

VERTICAL MODES FITTING

Considering an ocean under hydrostatic balance, continuously stratified, with rigid lid and flat bottom as boundary conditions for surface and bottom respectively, the linearized equations of motion can be decoupled into vertical and horizontal structures applying the method of variable separations, described in LeBlond & Mysak (1981). Then, an expression for the horizontal velocity vector can be written as

$$u(x, y, z, t) = \sum_{i=0}^{\infty} U_i(x, y, t) F_i(z), \qquad (1)$$

where U_i are the amplitudes of the *i-th* vertical mode, and F_i is the *i-th* vertical mode associated. The vertical modes F_i are calculated numerically by solving the eigenvalue equation

$$\frac{d}{dz} \frac{1}{N^2} \frac{dF_i}{dz} + \lambda_i F_i = 0, \qquad (2)$$

Table 2. General information about the moorings used on this study.

Mooring name	Period	Location	Local depth [m]	Reference
MARLIM[*]	1992/07/01 - 1992/11/27	40°W - 22.4°S	1059	Silveira et al. (2008)
F2200	2008/12/01 - 2009/11/30	42.9°W - 25.8°S	2237	Belo & Silveira (2013)
C3	1992/12/21 - 1994/03/20	44.9°W - 25.5°S	1261	Rocha et al. (2014)
BM334	1991/01/10 - 1992/11/23	46.7°W - 27.9°S	1113	Müller et al. (1998)

[*]Extracted from Silveira et al. (2008).

where N^2 is the stratification, and λ the eigenvalues. The boundary condition for F_i is flat bottom and rigid lid, and is given by

$$\frac{dF_i}{dz} = 0; z = (-H, 0). \qquad (3)$$

Each vertical mode obtained is vertically orthogonal to one another and is normalized to have unit magnitude when projected onto itself. Considering that the study region includes the continental slope and the SPP, we assumed this condition by solving a one-dimension case at each grid point to satisfy the local flat bottom boundary condition. According to Szuts et al. (2012), there are two methods to numerically fit the dynamical modes onto vertical profiles. The first one is the integral method, which is made by solving Eq. (1), and the second is using an inverse method generally based on point measurements. The integral method is commonly applied to continuous CTD/velocity profiles that have a very fine and uniform vertical resolution (*e.g,* Urbano Neto & Silveira (2003)).

The second method is the Gauss-Markov method, first proposed by Wunsch (1997), which allows more physical specifications to be included. This method is typically used for current meters that have only a few instruments on each mooring at unequal vertical spacing (*e.g,* Rocha et al. (2014)). Following this method, the Eq. (1) can be rewritten algebraically as

$$AU + \epsilon = B. \qquad (4)$$

The matrix A is the basis function matrix. It is Z x M in size, where M is the number of modes considered in the approximation and Z the number of vertical levels; U is a column vector of the M modal amplitudes to be determined; ϵ is a column vector of error; and B is a column vector of the Z observations of u. In contrast to a least-square solution, the Gauss-Markov estimate minimizes the variance of the fit and thus gives a more stable estimate (Szuts et al. 2012). For this case, the modal amplitudes are then found by

$$U = W_0 A^T \left(A W_0 A^T + I_z \sigma^2 \right)^{-1} B, \qquad (5)$$

where I_z is an identity matrix of size z, σ^2 is the accuracy of the records, and W_0 a diagonal matrix representing the *a priori* kinetic energy partition among the modes. According to Wunsch (1997), W_0 can be obtained by

$$W_0 = E_u^2 diag \left[w_0, w_1, w_2, w_3, w_4, w_5 \right] / \sum_{i=0}^{5} w_i, \qquad (6)$$

an example of a six mode truncation projection. Here, E_u^2 is an estimate of the total variance in the records, calculated from the observed data itself, and $\sum_{i=0}^{5} w_i$ is the sum of the *a priori* weights. Also we assume *a priori* that the vertical partitioning of the kinetic energy among the linear modes was in the ratio $w_0 : w_1 : w_2 : w_3 : w_4 : w_5$ from zeroth (barotropic) to fifth baroclinic modes. In the work of Wunsch (1997), this ratio was 1:1:1/2:1/4:1/8:1/16.

This method has previously been applied for moored current data at SB in the works of Rocha et al. (2014) and Biló et al. (2014). In this study, we followed the same procedure of Wunsch (1997) to describe the modal composition of the LADCP/CTD observed sections, and adopted the weight scheme of Eq. (6) to extrapolate the velocity field.

MODAL STRUCTURE OF SOUTH BRAZIL BIGHT

In this section, we aim to provide a general overview of the modal velocity structure in the SBB based on the quasi-synoptic velocity observations. First, we describe the circulation pattern and then discuss

the obtained modal velocity structure.

Quasi-synoptic circulation patterns

The surface quasi-synoptic circulation derived from altimeter and the vertical sections observed during the cruises are depicted in Figure 2. From the surface circulation (Figure 2a), we observe that during the CERESV cruise, the BC is entering in the SBB with its jet confined to the slope, with a cyclonic meander being formed at 24°S - 43°W. The observed cross-sectional speeds from LADCP (Figure 2b) shows a shallow BC with its jet carrying 6.2 Sv (1 Sv = 10^6 m^3 s^{-1}) and essentially confined in approximately 500-600 m of water column, with velocities that exceed 0.80 m s^{-1}. From the isoneutral contours (Figure 2c), we observe that the BC is responsible for carrying both TW and SACW into the SBB. We also note the equatorward flow originated from the IWBC between the depths of 700 m and 1100 m, in the outermost portion of the slope ($\sim$100 km away). In this scenario, the IWBC transports approximately 1.1 Sv with a maximum speed of 0.39 m s^{-1}.

Now we analyze a second cross-section current pattern carried out in the southern portion of the SPP, obtained during the CERESIV cruise. The surface circulation (Figure 2d) in the SBB shows the BC flow and the presence of an anticyclone slightly south of the oceanographic transect. The presence of this anticyclone is responsible for displacing the BC core onshore, as can be noted on Figure 2e. The observed BC jet has speeds that exceed 0.45 m s^{-1}, and transports 5.3 Sv. Located on the innermost portion of the continental slope, the BC has a vertical extension of approximately 500 m in depth and is responsible for the advection of both TW and SACW (Figure 2f). The presence of the IWBC just south of the SPP could also be verified confined to the continental slope between 500 m and 1500 m depth. At its core, we observe velocity values above 0.15 m s^{-1}.

It is already well established that the BC system presents an intense mesoscale activity, producing features such as meanders, eddies and dipoles, as demonstrated by observational evidence (Campos et al. 2000, Calado et al. 2006, Silveira et al. 2008). The presence of Agulhas Rings arriving at the SBB

was previously reported in the works of Guerra et al. (2018) and Laxenaire et al. (2018). The CERESIII cruise sampled one large anticyclonic eddy while it was interacting with a cyclonic eddy in the SPP area (Figure 2g).

The along-section velocity structure shows that these rings can reach more than 2000 m (Figure 2h) with maximum velocities of $\sim$0.3 m s^{-1} near the surface and a secondary intermediate core of $\sim$0.2 m s^{-1} between 500-1000 m. Near the bottom, there is an intensification of the northward directed flow with values comparable to those at the surface. Also, there is a flow inversion on the onshore lobe between 1750 m and the bottom, these features are expected and may be due to the bottom friction. Therefore, the huge vertical extension of this feature is responsible for recirculating all the observed water masses in the same sense (Figure 2i).

Another mesoscale structure fully sampled from surface to bottom in the SBB was a cyclonic meander originated from the BC near the Cape Santa Marta, during the MR03 cruise (Figure 2j). The observed meandering BC presented its core above the 2500 m isobath, which was merged with the cyclonic offshore lobe. The cross-sectional velocity structure (Figure 2k) shows near surface southward velocities above 0.6 m s^{-1} on the offshore lobe, while on the onshore lobe the maximum observed velocities were 0.18 m s^{-1} northward. In this transect, surface (TW and SACW), intermediate (AAIW), and deep waters (UCDW and NADW) were found inside the meander extension (Figure 2l).

Modal composition of observed velocity fields

Figure 3 displays a comparison between the observed velocity and the modal projections of the velocity profiles with an increase in the number of modes used (from i = 0 to 2, 4 and 6). For the CERESV cruise, the barotropic velocity estimates (Figure 3b) resemble an almost southward flow associated with the presence of the BC over the continental slope. However, this southward barotropic flow is responsible for only 15% of the observed velocity structure. Considering the addition of the first baroclinic mode in the velocity projection (Figure 3c), the explained variance increases
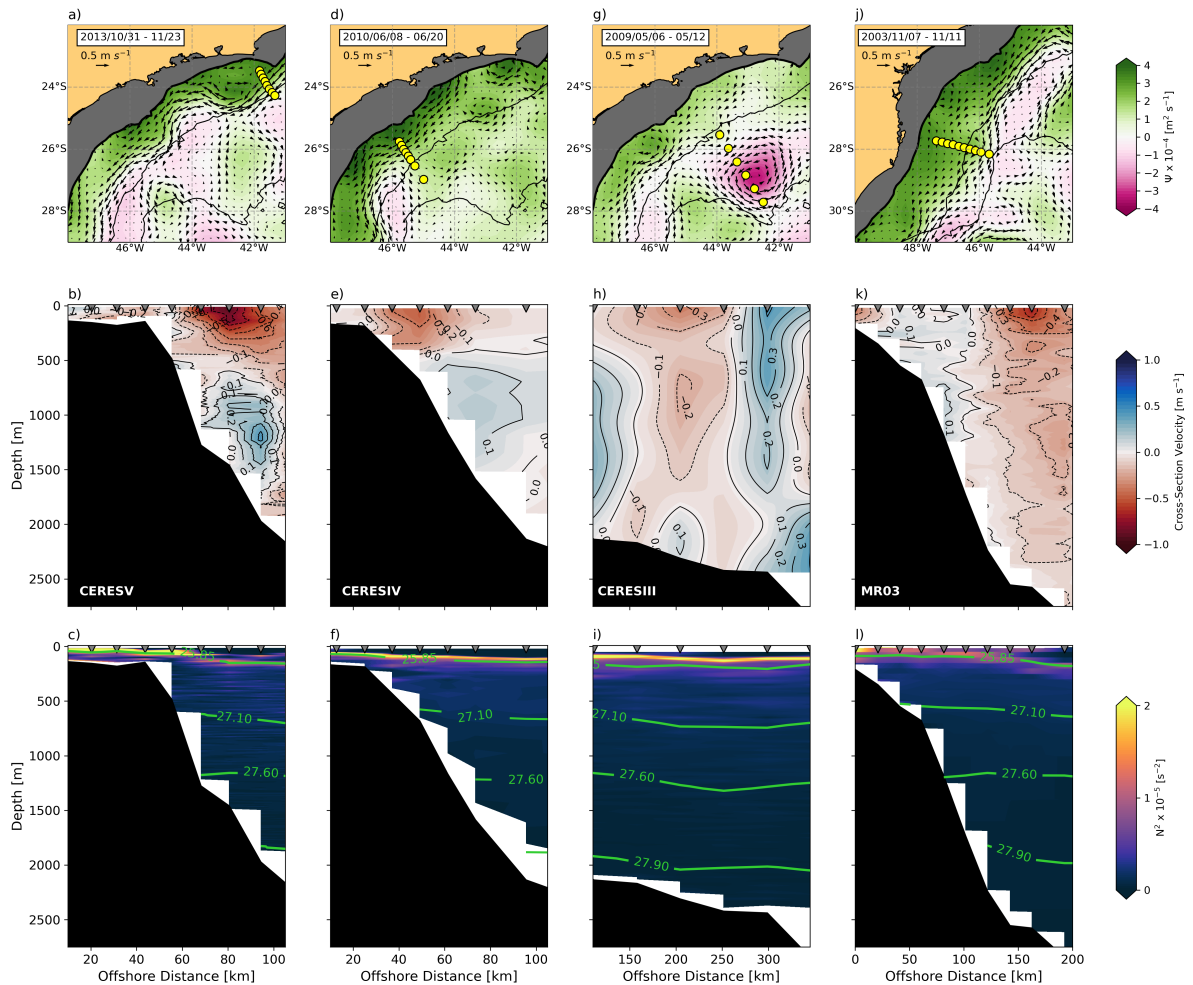
Figure 2. General quasi-synoptic scenario for the transects used in this study. Top row shows the mean surface stream function and geostrophic velocity vectors delivered from altimeter during the period of each transect; middle row shows the cross-sectional velocity from LADCP at each section; bottom row displays the stratification (N^2) frequency obtained from the *in situ* CTD casts and green lines denote the water mass interfaces according to Valla et al. (2018). Black contours on top row subplots are the 100, 2000 and 3000 m isobaths.

to 62%. This result shows that the BC-IWBC system is mainly dominated by the two first dynamical modes, in agreement with earlier studies (Silveira et al. 2000, Fernandes et al. 2009). Using a total of 4 and 6 dynamical modes, the explained variance increases to 75% and 84%, respectively (Figures 3d and 3e).

Barotropic velocities for the CERESIV cruise (Figure 3g) show a different pattern in comparison to the scenario of the Cape Frio transect (Figure 3b). On the inner slope, there is a southward flow with velocities that exceed $0.3\,\mathrm{m\,s^{-1}}$ located near the BC core, while for distances beyond 60 km, there is a northward oriented flow with velocities exceeding $0.07\,\mathrm{m\,s^{-1}}$ due the IWBC presence. This difference may arise due to the fact that in Figure 3a, both observed BC and IWBC cores are vertically aligned, while on Figure 3f they are vertically shifted. This fact also reflects on the contribution of the barotropic mode in the latter section: it explains approximately 31% of the observed velocity variance. The increasing importance of the barotropic mode in this scenario is due to the impinging of the BC onto the shelf break and upper slope. Both, the barotropic and the first baroclinic mode explain approximately 67% of the velocity variance (Figure 3h). Using 4 dynamic modes, the explained variance percentage goes to 86% (Figure 3i), and using 6 dynamic modes, it increases to 90% (Figure 3j).

Unlike what was observed in the two previous transects for the BC system, the anticyclone modal structure observed on CERESIII cruise shows that the barotropic mode is responsible for nearly 50% of the observed velocity structure (Figure 3l). The inclusion of the first baroclinic mode reproduces the surface intensification (Figure 3m) and increases the explained variance to 64%. Finally, the secondary velocity core, located between 500 m and 1000 m is recovered when we include 4 dynamic modes on the projection (Figure 3n) and the explained variance increases to 80%. Using 6 dynamic modes, this percentage increases to 87% (Figure 3o) and the obtained structure is quite similar to the one reproduced with 4 modes.

The cyclonic meander observed on MR03 cruise also presents relevant barotropicity, as can be seen on the barotropic velocity projection (Figure 3q), which explains 46% of the observed variance. With the first baroclinic mode included, this percentage goes to 71%, and this mode reproduces the observed surface intensification on the offshore lobe of the meander (Figure 3r). Using 4 dynamical modes, the explained variance increases to 79% (Figure 3s). With 6 dynamical modes (Figure 3t), the secondary velocity core in intermediate depths on the offshore lobe is reproduced, and the explained variance increases to 82%.

Both mesoscale structures of the Agulhas ring and Cape Santa Marta meander analyzed in this study ocupy the whole water column. Therefore, they present a notable barotropic component. However, in the BC system, the vertical shear between the BC and IWBC introduces a relevance to the first baroclinic mode on the velocity projections. For both scenarios, these two modes together explained the majority (> 60%)of the variance in all the described transects.

VERTICAL EXTRAPOLATION

In this section, we present the results obtained on the sensitivity test of the extrapolated velocity fields. This extrapolation is made performing the following procedure: (i) obtain the *in situ* N^2 profile at each CTD station and apply Eq. (2) to compute the vertical dynamic modes; (ii) exclude all LADCP velocity data below 600 m, which is the nominal depth that 75 kHz VMADCP can reach; (iii) select only the N^2 and LADCP data above 600 m to perform the mode-fitting in Eq. (1); (iv) use the obtained amplitudes multiplied by a weight scheme obtained from mooring data to recover the velocity profile using the modal re-composition.

Weight Scheme

As observed previously, the first two dynamical modes (barotropic and 1st baroclinic) are responsible for recovering more than 60% of all the observed structures in the SBB, reinforcing the importance of these two fundamental dynamical modes. However, a more detailed reproduction (> 80%) is recovered using 6 modes in all the transects analyzed.

To provide a general overview and obtain a weight scheme to extrapolate the LADCP velocity profiles, we define as a typical profile those that
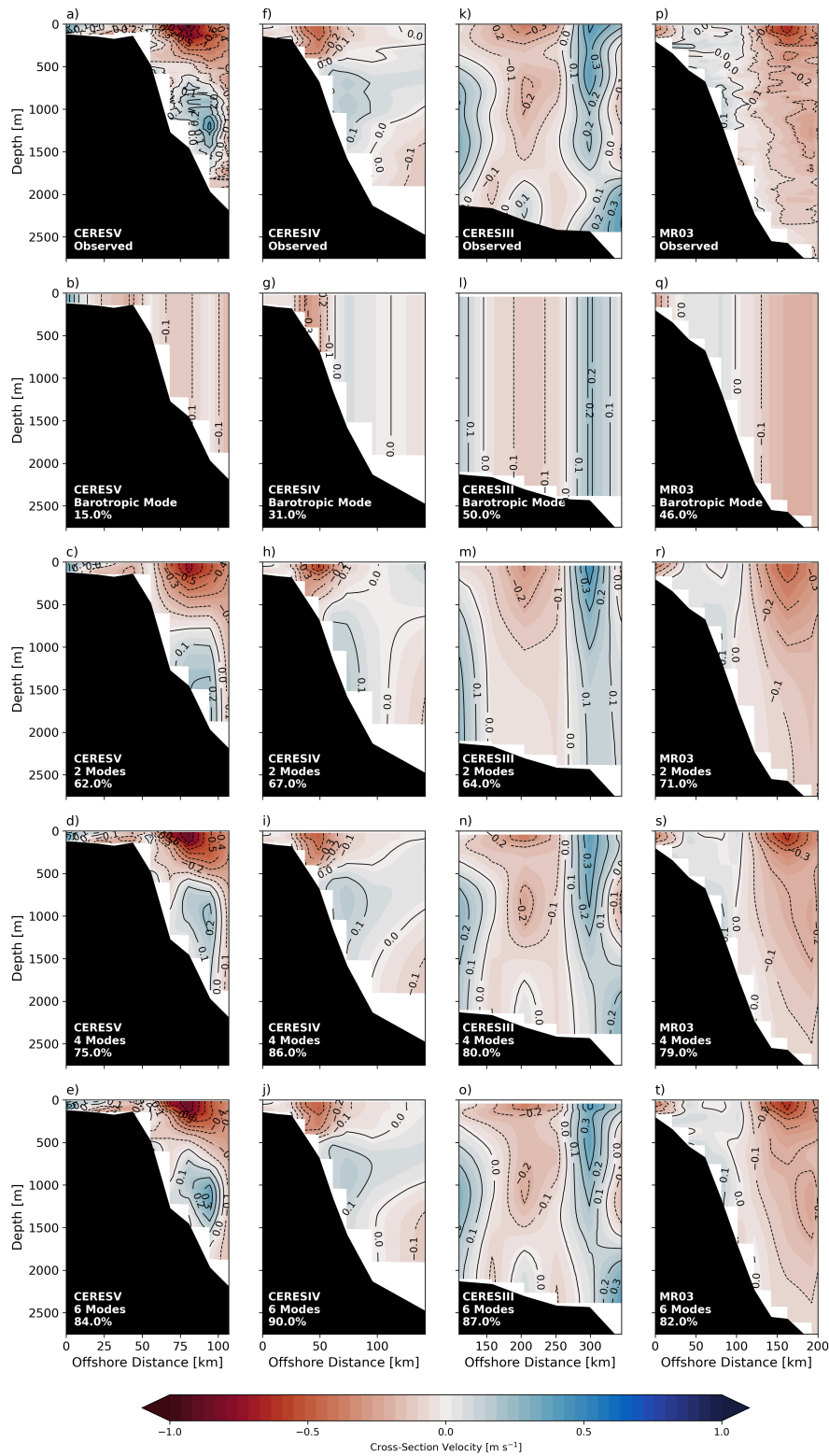
Figure 3. Observed and mode-projected velocities for the LADCP velocity profiles. First row shows the cross-sectional velocities for each cruise. The following rows shows the mode projected velocities with the number of modes labeled on each subplot.

describe the main characteristics of both BC-IWBC vertical shear, the barotropicity of the vortical structures and their surface intensification. These profiles were obtained from the moorings listed on Table 2. For the MARLIM and C3 moorings, we adopt their mean along-slope velocity as being characteristic of the observed current pattern. Hence, both are located in areas where the main flow is characterized by the BC system. For those moorings located in areas of intense mesoscale variability (F2200 and BM334), we obtain their first Empirical Orthogonal Function (EOF) mode, and adopt it as being characteristic of the structures that acts in each site. For the F2200 mooring, the first EOF mode explains approximately 78% of the series variance, and for the BM334 mooring, the first EOF accounts for 74% of flow variability.

All these profiles are interpolated to a 5-m regular grid, smoothed using a running mean of 19-points, and normalized by dividing the profile by its maximum value (Figure 5). We follow Mueller (2013), who first used normalized data from ADCP river discharge measurements on channels to extrapolate its records. According to Mueller (2013), for the case of discharge, the normalization procedure ensures that data is plotted in the correct position along the discharge profile in relation to the streambed. Here, the mean normalized profile minimizes the effect of noisy data, and is consistent with the mean current structure. After normalizing the profile data, we project the six dynamical modes obtained from WOA2018 $N^2(z)$ profiles at each mooring location (Figure 4) into their structure (Figure 5). Then, we evaluate their relative individual contribution on the reconstruction to use as a weight matrix (Eq. 6).

We use the weight scheme for each mooring listed on Table 3 to extrapolate the velocity profiles
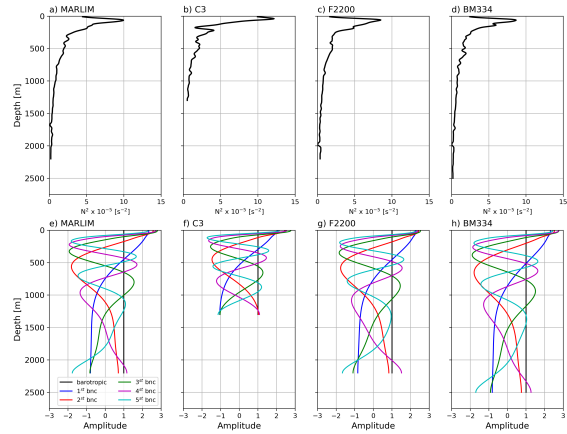
Figure 4. Climatological N^2 profiles obtained from WOA2018 at each mooring location (a - d); The first six dynamical modes, i.e barotropic and five baroclinics (bnc) obtained from WOA2018 at each mooring location (e - h).
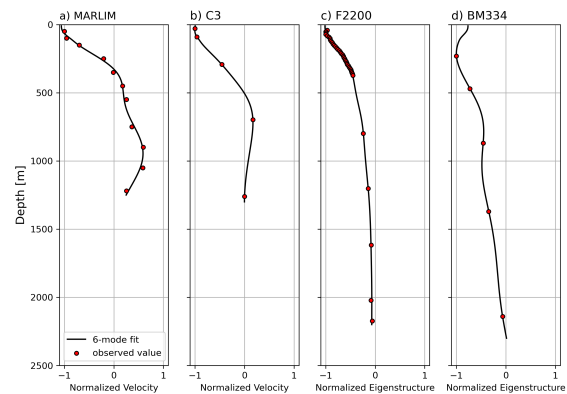
Figure 5. Characteristic profiles obtained for the mean along-slope velocity normalized at each mooring: a) MARLIM * (22.4°S); b) C3 (25.5°S) ; c) F2200 (25.8°S); d) BM334 (27.9°S).*The MARLIM mooring average profile was extracted from Silveira et al. (2008).

Table 3. Approximated relative contributions of each mode to reconstruct the profiles on Figure 5. These values were used as a weight scheme from Eq. (6) to extrapolated velocity data

Mode	MARLIM (22.4°S)	C3 (25.5°S)	F2200 (25.8°S)	BM334 (27.9°S)
0	0.25	0.20	1.00	1.00
1	1.00	1.00	0.70	0.15
2	0.01	0.10	0.01	0.06
3	0.01	0.01	0.01	0.06
4	0.01	0.01	0.01	0.06
5	0.01	0.01	0.01	0.06

for each LADCP transect according to the closest mooring mean profile available. For the CERESV cruise, we use the MARLIM mooring; for CERESIV, the C3 mooring; for CERESIII, the F2200 mooring and for MR04 we use the BM334 mooring.

COMPARISON BETWEEN EXTRAPOLATED AND OBSERVED FIELDS

A comparison between the extrapolated profiles obtained and the observed ones can be seen on Figure 6a - 6l. These results show that this method is able to recover the majority of the observed vertical structure, especially the vertical shear and flow inversion on the BC system transects (Figures 6b and 6e), and the mesoscale eddy structure occupying the whole water column (Figures 6h and 6k). For the CERESV and CERESIII extrapolated transects (Figure 6b and 6h), the major differences occurred near the bottom, where we find root squared errors (RSE) of above $0.4\,\mathrm{m\,s^{-1}}$ (Figures 6c and 6i). For the case of CERESIV transect, higher RSE are found on the innermost portion of the slope (Figure 6f) due the fact that the extrapolation produced a slightly faster IWBC. Finally, for the extrapolated meandering BC (Figure 6k), higher errors are obtained due the fact that the extrapolation does not reproduce perfectly the onshore lobe of the cyclone. The procedure also generates a faster and shallower mid-depth velocity core on the offshore lobe in comparison with the observed one (Figure 6l). Even if punctual extrapolated values exceed $0.4\,\mathrm{m\,s^{-1}}$ in difference relative to the observed field, the average root mean square error (RMSE) for all extrapolated transects is below $10^{-2}\,\mathrm{m\,s^{-1}}$ (Figure 7a). The normalized root mean square error (nRMSE), the mean percentage for the error values are less than 10% in all the transects (Figure 7b). Furthermore, in order to understand the RSE distribution, their cumulative density function (CDF) shows that the majority (> 60%) of error values are less than $0.1\,\mathrm{m\,s^{-1}}$, with an exception for the CERESIV transect, where more than 60% of the values are below $0.14\,\mathrm{m\,s^{-1}}$ (Figure 7c).

While the RMSE-related values evaluate amplitude relationships between observed and extrapolated fields, correlation-related values evaluate the phase differences. In other words, we choose corre-

lation to evaluate the ability of modal extrapolation to preserve the horizontal velocity gradients and the velocity signal. Therefore, if horizontal velocity gradients are in agreement, there should be a positive correlation. For the opposite, a negative correlation must be indicative that horizontal gradients are not being preserved, and opposite velocities signal may have appeared during the extrapolation.

On the left column of Figure 8, we plot the correlation for each z-level between observed and extrapolated velocity transects. Positive and strong correlations are observed at the Cape Frio transect (CERESV) from 600 m to 1500 m, with strong negative correlations (Figure 8a), and no significant velocity inversions are observed. A linear regression between observed and predicted velocities by the extrapolation shows a correlation coefficient of 0.86 between these variables (Figure 8b).

Furthermore, the use of radar diagrams helps us to verify dynamic similarities between the extrapolated and observed features, allowing us to compare different variables in each panel. On the right column of Figure 8, we compare the relative values for currents core velocity ($\mathrm{m\,s^{-1}}$), its offshore distance (km), transport (Sv), and associated depth (m). For the BC-IWBC transects (CERESIV and CERESV), the analyzed feature is the IWBC jet, while for the CERESIII and MR03 transects we analyze the onshore and offshore lobe of the eddies. On the CERESV cruise, the extrapolation produces an IWBC with a core slightly faster ($0.41\,\mathrm{m\,s^{-1}}$ against $0.39\,\mathrm{m\,s^{-1}}$) with a difference of 1,6 Sv in its transport, but is able to reproduce the offshore distance and depth of the current core (Figure 8c).

For the transect obtained during the CERESIV cruise, the extrapolated results present a moderate correlation on the horizontal only between 660 m and 810 m, where the scheme produces a narrower and faster IWBC core in comparison to observations (Figure 8d). This transect presents strong correlation on depths above 1000 m, and the full section correlation shows a correlation coefficient of 0.93 (Figure 8e). Radar diagrams show that the overestimation on velocity is of $0.03\,\mathrm{m\,s^{-1}}$ and the produced IWBC core is 3 km closer to the shore and 50 m deeper in comparison to the observed field. The obtained difference on the transport is about 0.2 Sv. It is worth noticing that the extrapo-
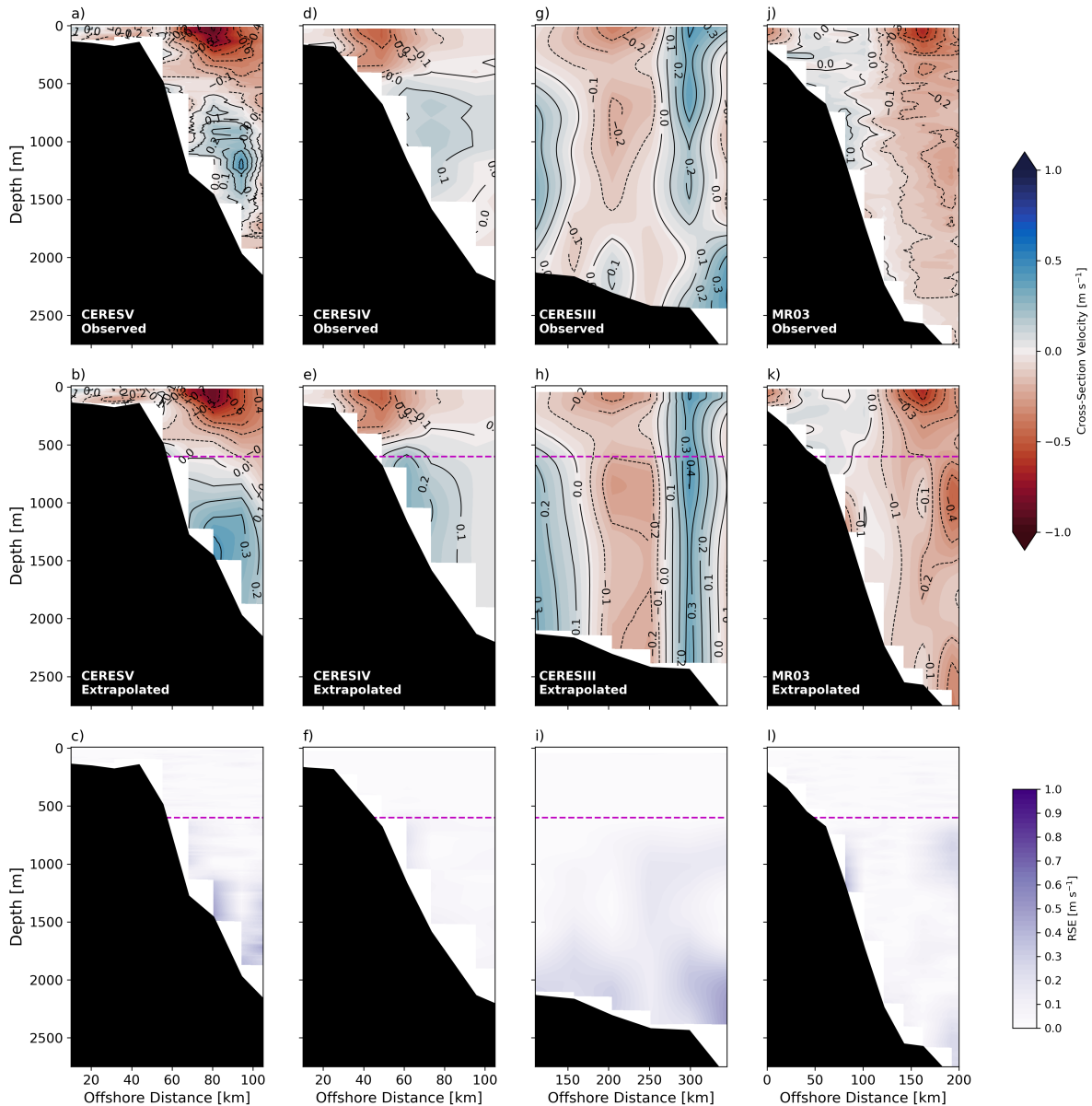
Figure 6. Observed (top row) and mode-projected velocities (mid row) along with their root squared error (RME, bottom row) for each velocity transect. Magenta horizontal dashed line on mid and bottom rows marks the depths in which observed velocity data below this line was excluded.

lated results obtained for this transect is qualitatively similar to the ones obtained by Biló et al. (2014). The authors estimated the geostrophic velocity from Expendable Bathythermograph (XBT) data in this transect using a linear relationship between temperature and specific volume anomaly and their results are similar to the ones presented here (please see the displacements of the 0.1 and 0.2 m s⁻¹ isotachs

on Figure 13 from Biló et al. (2014)).

The extrapolation of the anticyclone captured on CERESIII cruise shows that the barotropic structure of the eddy is recovered and that its velocity core between 500 m and 1000 m has also appeared (Figure 6h). Errors are higher for depths above 2000 m, where the extrapolation failed on recovering the horizontal velocity pattern, and no positive significant
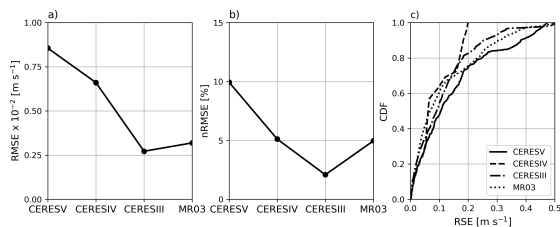
Figure 7. a) Obtained root mean square error (RMSE) between the observed and extrapolated transects; b) the respective normalized root mean square error(nRMSE); c) Cumulative Density Functions (CDF) for the root square error obtained in each transect.

correlation is found (Figure 8g). This issue may be due to the fact that the observed section contains velocity inversions near the bottom. Despite that, the extrapolated field presented an r of 0.78 (Figure 8h). On the radar diagram (Figure 8i), the characteristics of both eddy lobes (onshore lobe in red and offshore lobe in blue) are plotted. The fact that the extrapolated transect does not reproduce the velocity inversions near the bottom reflects on an overestimation of the transport for both lobes, where they increased to ~30% the observed transport in this portion of the water column. Despite this fact, the differences obtained for the other parameters, such as core depth and distance were near 10%.

For the cyclonic meandering BC captured during the MR03 cruise, the extrapolation is able to reproduce the full-depth offshore lobe of the meander, which is fused with the BC axis (Figure 6k). For the onshore lobe, it is not fully reproduced, especially near the slope, where extrapolated velocities present an inverse signal in comparison to the observed (i.e. northward flow). This inverse signal results in the depth interval between 1000 m and 1800 m being dominated by low correlation positive coefficients (Figure 8j), and below that, positive and significant coefficients are obtained. This section presents a Pearson coefficient of 0.78 (Figure 8k). Despite the transport of the offshore lobe, which is overestimated at 22%, all other parameters in this lobe remain with a difference less than 2% in comparison to the observed (red lines on Figure 8). However, the fact that the onshore lobe was not fully reconstructed on the extrapolation, gives rise

to an underestimate of 40% for the onshore lobe transport, on the maximum velocity, and its associated depth. A quantitative assessment between the parameters plotted on the radar panels of Figure 8 is displayed in Table 4.

In the work of Biló et al. (2014), the authors proposed direct methods for estimating geostrophic velocities for the BC-IWBC system. Their calculated transports for the IWBC domain, the obtained values underestimated (overestimated) the observed transport in ~50% using referenced geostrophic method that combined VMADCP and CTD profiles (VMADCP and only temperature profiles). Despite these differences between the observed and predicted values, the authors concluded that large uncertainties are involved in the geostrophic calculations, but all of their proposed methods agree well with the directly observed velocity field. In our study, we also observe that the extrapolated sections are in good qualitative and quantitative agreement with the directly observed velocity field from LADCP measurements, suggesting that this dynamic approach can be a useful tool to perform a first assessment of quasi-geostrophic circulation in the SBB.

EXTRAPOLATION WITH VMADCP DATA

In the previous section, we presented a comparative scenario between observed and the extrapolated data, in which we excluded all data bellow 600 m to mimic a limited acquisition from VMADCPs. In this section, we will show the results of applying the extrapolation method on three velocity transects acquired by 75 kHz Teledyne VMADCP. The vertical VMADCP cell spacing was 10 m, and current velocity information was obtained from long-time average data and processed with the Common Ocean Data Access System software (CODAS). These transects were obtained during the Santos Project Experiment funded by PETROBRAS. The quasi-synoptic surveys and their corresponding surface circulation scenarios depicted from altimetry are presented on Figure 9.

The transect B2021 was done between the days of 2021/12/26 - 28 and captured part of the BC just south of a cyclonic meander that was attached to the current while being advected southward (Fig-
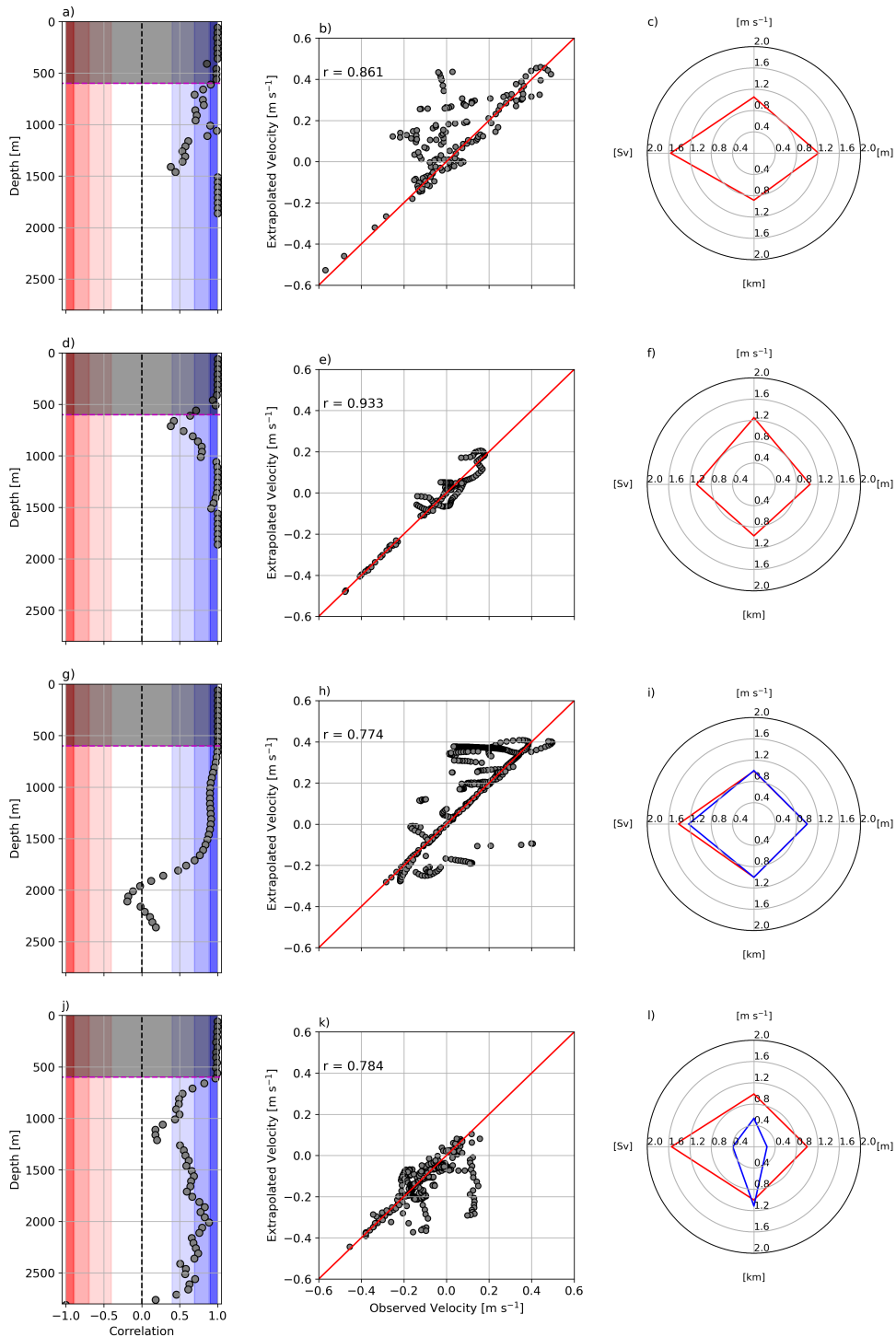
Figure 8. Comparison between observed and extrapolated velocities for the LADCP transects. Each row refers for the respective cruises: CERESV; CERESIV; CERESIII and MR03. On left column panels are plotted the correlation in each depth level; central column panels shows the scatterplot of entire transects and right columns are the normalized radar diagrams for the following extrapolated variables: velocity core (m s^{-1}); core depth (m); core distance (km) and current transport (Sv). On (c) and (f) these values are for IWBC (redlines) and for (i) and (l) they are for eddies southward flow (red) and northward flow (blue). Magenta horizontal dashed lines on left column marks the depth in which observed velocity data was excluded.

ure 9a). In this scenario, the BC is split into two branches. The onshore branch is the BC itself while the offshore branch is part of the meander (Figure 10a). The transect E2019 (2019/07/01 - 06) captures an anticyclonic eddy in its almost full horizontal extension as well as the BC flowing to the south (Figure 9b), with its core interacting with the western portion of the eddy. Finally, the transect G2022 (2022/03/23 - 26) captured a Cape Frio cyclonic meander while it was still attached to the BC (Figure 9c).

In the observed velocity from transect B2021 (Figure 10a), the BC core is displaced in an offshore direction ($\sim$80 km), with surface velocities that exceed $0.3\,\mathrm{m\,s^{-1}}$. Such displacement occurs due to the presence of the cyclonic meander. Finally, below 1000 m, we can see an organized northward flow probably associated with the IWBC, that was partially sampled by the VMADCP. The extrapolated VMADCP section, using the C3 weight scheme (second column of Table 3), is able to extend the velocity field to the depth of the CTDs stations (Figure 10d). The resulting velocity pattern reproduces a similar northward flow below 1000 m, indicative of the IWBC presence.

In the transect E2019 the VMADCP was able to sample velocity in the upper $\sim$800 m of the water column (Figure 10b). The observed field shows the onshore lobe of the anticyclone merged with the BC flow, with intensified velocities near the surface ($>0.3\,\mathrm{m\,s^{-1}}$). The offshore lobe of the anticyclone has a surface velocity structure similar to the onshore, but less intense (maximum values $<$ $0.3\,\mathrm{m\,s^{-1}}$). Also, confined to the innermost portion of the slope, centered at $\sim$700 m, there is the IWBC flowing northward. The extrapolated velocity field using the F2200 weight scheme (3rd column on Table 3), for this transect (Figure 10e), is able to

reproduce the main observed velocity patterns, i.e., the narrower IWBC flow confined to the inner slope and a most deeper and intense onshore lobe in comparison to the offshore one in the anticyclone.

Finally, for transect G2022, which essentially sampled a Cape Frio eddy while attached to BC, the observed velocity pattern (Figure 10c) shows a cyclone of nearly 130 km in diameter, with its velocity core located near the surface. This structure seems to have an important barotropicity and probably reaches deeper depths beyond the instruments detection limit. This structure is quite similar to the mesoscale vortical structure observed on Figures 3k and 3p, in which LADCP transects showed the importance of barotropicty for both cyclones and anticyclones. Hence, we adopted the BM334 mooring weight scheme (the same used to extrapolate the velocity field of the cyclone from MR03 cruise and displayed on the fourth column on Table 3) to extrapolate the observed velocity. The obtained results are in Figure 10h. The extrapolated field produces a structure that occupies the entire water column. This is somewhat expected, hence the barotropic mode was the most important on the weight scheme adopted for this case. Another relevant aspect obtained on the extrapolated field was an intensification of the velocities on the offshore lobe of the cyclone. Considering that this depth is outside the limits of instrument detection, we cannot argue about wether this pattern is a method issue or a real feature that could be presented on the observed field if this depth was reached. Nevertheless, it is interesting to note that on the observed field, the $0.1\,\mathrm{m\,s^{-1}}$ isotach may extend deeper than the instrument detection limit (Figure 10c). Despite that, we can also argue about the limitations of our technique and its inherent sensitivity, which are discussed in the Supplementary Material.

Table 4. Comparison between observed and extrapolated values that were normalized on the radar diagram on Figure 8. For the mesoscale eddy columns, values in parenthesis are the ones for the offshore lobe of the structure, and values outside the parenthesis are for the onshore lobe.

	Intermediate Western Boundary Current				Mesoscale Eddy			
	CERESV		CERESIV		CERESIII		MR03	
	Observed	Extrapolated	Observed	Extrapolated	Obsserved	Extrapolated	Observed	Extrapolated
Max Velocity (m s^{-1})	0.39	0.41	0.17	0.21	0.39 (0.33)	0.39 (0.33)	0.10 (0.61)	0.05 (0.60)
Core Distance (km)	93.29	82.42	73.22	70.82	301.53 (201.99)	301.53 (201.99)	87.22 (161.98)	97.18 (161.98)
Core Depth (m)	1194.42	1448.02	940.82	991.54	78.58 (78.58)	78.58 (78.58)	940.82 (78.58)	230.75 (78.58)
Transport (Sv)	2.85	4.46	2.59	2.79	23.66 (23.40)	29.29 (31.82)	0.82 (33.85)	0.32 (46.06)
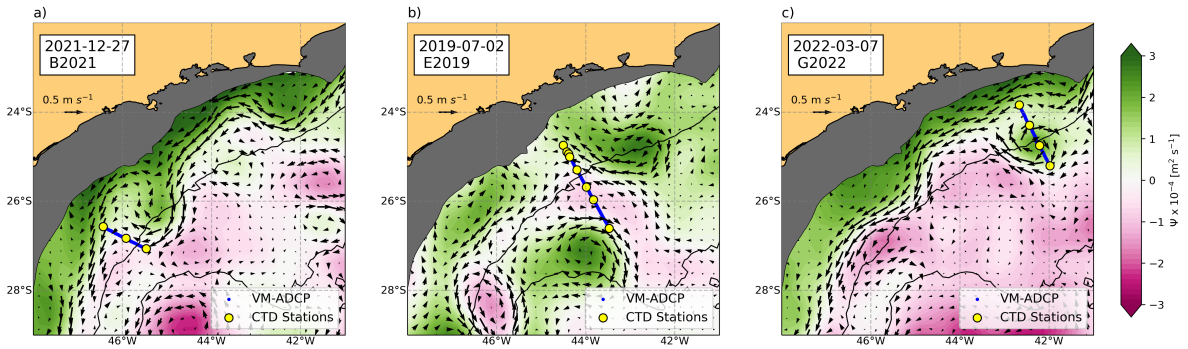
Figure 9. Daily stream function derived from altimetric data which represents the synoptic circulation observed during the realization of each section with geostrophic velocity vectors. Black contours are the 100, 2000, and 3000 m isobaths.
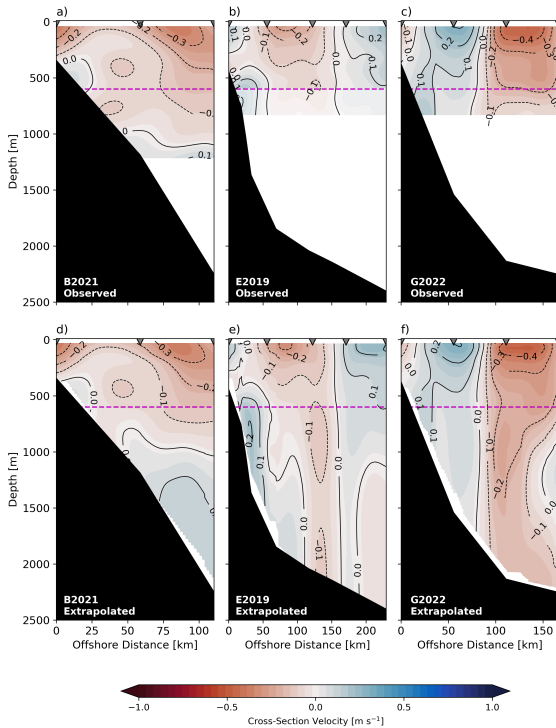
Figure 10. Cross-sectional velocity observed from VMADCP (top row) and extrapolated estimates (bottom row) using the modal extrapolation. Magenta dashed lines denote the depth in which velocity data was excluded and gray triangles are the CTD stations.

SUMMARY AND FINAL REMARKS

In this study, we adapted a method of extrapolation previously used for current meter data to quasi-synoptic velocity measurements obtained in the SBB. An independent set of average vertical profiles from moorings was used as a basis to obtain an estimate of the vertical contribution from each dynamical mode. The modes were calculated from climatological WOA2018 profiles. It's worth reinforcing that during this extrapolation procedure, we maintained the constraint that the relative importance of the two first dynamical modes was higher in comparison to the others.

The contribution of each dynamic mode was used as a weight scheme to extrapolate the velocity measurements. Initially, this was applied to four transects obtained with LADCP, each one sampling a different dynamic pattern in the SBB. In these transects, all velocity data below 600 m was excluded to mimic an acquisition made by 75 kHz VMADCP. The extrapolation produced velocity patterns that were in agreement with the observed flow structures, as depicted on radar plots. Also, all the extrapolated results remained with a nRMSE less than 10%.

After comparing and validating the method, we applied it to observed 75 kHz VMADCP data, being able to extrapolate the measurements to the depth of the CTD stations. In a region where the oil and gas industry is highly active, such as the SBB, observations made by VMADCP are easier to perform and more frequent than LADCP profiling. However, VMADCP instruments often present a limited vertical coverage, depending upon their operating frequency. Thus, our results suggest that this dynamic approach can be a useful tool to extrapolate VMADCP data beyond the limits of detection from

the equipment, performing a first assessment of the circulation in the SBB. We also believe that future improvements of this technique can be achieved by combining this dynamical technique with statistics and improved logic derived from machine learning and artificial intelligence algorithms, using a more extended dataset (*e.g,* synthetic data from ocean model outputs).

ACKNOWLEDGMENTS

REFERENCES

BELO, W. & SILVEIRA, I. 2013. A variabilidade vertical do oceano na Bacia de Santos, *Boletim de Geociências da Petrobras* **21**: 39–62.

BILÓ, T. C., DA SILVEIRA, I. C. A., BELO, W. C., DE CASTRO, B. M. & PIOLA, A. R. 2014. Methods for estimating the velocities of the Brazil Current in the pre-salt reservoir area off southeast Brazil (23°S–26°S), *Ocean Dynamics* **64**(10): 1431–1446.

BOEBEL, O., DAVIS, R., OLLITRAULT, M., PETERSON, R., RICHARDSON, P., SCHMID, C. & ZENK, W. 1999. The intermediate depth circulation of the western South Atlantic, *Geophysical Research Letters* **26**(21): 3329–3332.

BOYER, T., GARCIA, H., LOCARNINI, R., ZWENG, M., MISHONOV, A., REAGAN, J., WEATHERS, K., BARANOVA, O., SEIDOV, D. & SMOLYAR, I. 2018. World Ocean Atlas 2018.

CALADO, L., GANGOPADHYAY, A. & DA SILVEIRA, I. 2006. A parametric model for the Brazil Current meanders and eddies off southeastern Brazil, *Geophysical Research Letters* **33**(12).

CAMPOS, E. J. D., VELHOTE, D. & SILVEIRA, I. C. A. D. 2000. Shelf break upwelling driven by Brazil Current cyclonic meanders, *Geophysical Research Letters* **27**(6): 751–754.

COSTA, V. S., MILL, G. N., GABIOUX, M., GROSSMANN-MATHESON, G. S. & PAIVA, A. M. 2017. The recirculation of the intermediate western boundary current at the Tubarão Bight–Brazil, *Deep Sea Research Part I: Oceanographic Research Papers* **120**: 48–60.

DUARTE, C. S. & VIANA, A. R. 2007. Santos Drift System: stratigraphic organization and implications for late Cenozoic palaeocirculation in the Santos Basin, SW Atlantic Ocean, *Geological Society, London, Special Publications* **276**(1): 171–198.

FERNANDES, A. M., DA SILVEIRA, I. C., CALADO, L., CAMPOS, E. J. & PAIVA, A. M. 2009. A two-layer approximation to the Brazil Current–Intermediate Western Boundary Current System between 20°S and 28°S, *Ocean Modelling* **29**(2): 154–158.

FISCHER, J. & VISBECK, M. 1993. Deep velocity profiling with self-contained ADCPs, *Journal of Atmospheric and Oceanic Technology* **10**(5): 764–773.

GORDON, A. L. 1989. Brazil-Malvinas confluence–1984, *Deep Sea Research Part A. Oceanographic Research Papers* **36**(3): 359–384.

GUERRA, L. A. A., PAIVA, A. M. & CHASSIGNET, E. P. 2018. On the translation of Agulhas rings to the western South Atlantic Ocean, *Deep Sea Research Part I: Oceanographic Research Papers* **139**: 104–113.

LAXENAIRE, R., SPEICH, S., BLANKE, B., CHAIGNEAU, A., PEGLIASCO, C. & STEGNER, A. 2018. Anticyclonic eddies connecting

the western boundaries of Indian and Atlantic Oceans, *Journal of Geophysical Research: Oceans* **123**(11): 7651–7677.

LEBLOND, P. H. & MYSAK, L. A. 1981. *Waves in the Ocean*, Elsevier.

LEGEAIS, J.-F., OLLITRAULT, M. & ARHAN, M. 2013. Lagrangian observations in the Intermediate Western Boundary Current of the South Atlantic, *Deep-Sea Research* **85**: 109–126.

LEVITUS, S. 1982. *Climatological Atlas of the World Ocean*, Vol. 13, US Department of Commerce, National Oceanic and Atmospheric Administration.

LODER, J. W., BOICOURT, W. C. & SIMPSON, J. H. 1998. Western Ocean boundary shelves, *The Sea* **11**: 3–28.

LUKO, C. D., DA SILVEIRA, I., SIMOES-SOUSA, I. T., ARAUJO, J. M. & TANDON, A. 2021. Revisiting the Atlantic South Equatorial Current, *Journal of Geophysical Research: Oceans* **126**(7): e2021JC017387.

MCDOUGALL, T. J. & BARKER, P. M. 2011. Getting started with TEOS-10 and the Gibbs Seawater (GSW) oceanographic toolbox, *Scor/Iapso WG* **127**: 1–28.

MEISLING, K. E., COBBOLD, P. R. & MOUNT, V. S. 2001. Segmentation of an obliquely rifted margin, Campos and Santos basins, southeastern Brazil, *AAPG bulletin* **85**(11): 1903–1924.

MUELLER, D. S. 2013. extrap: Software to assist the selection of extrapolation methods for moving-boat ADCP streamflow measurements, *Computers & Geosciences* **54**: 211–218.

MÜLLER, T. J., IKEDA, Y., ZANGENBERG, N. & NONATO, L. V. 1998. Direct measurements of western boundary currents off Brazil between 20°S and 28°S, *Journal of Geophysical Research: Oceans* **103**(C3): 5429–5437.

PUJOL, M. & MERTZ, F. 2019. Product user manual for sea level SLA products, *Copernicus Marine Monitoring Service* .

ROCHA, C. B., SILVEIRA, I. C. A. D., CASTRO, B. M. & LIMA, J. A. M. 2014. Vertical structure, energetics, and dynamics of the Brazil Current System at 22 °S–28 °S, *Journal of Geophysical Research: Oceans* **119**(1): 52–69.

SILVEIRA, I. C. A. D., CALADO, L., CASTRO, B., CIRANO, M., LIMA, J. & MASCARENHAS, A. D. S. 2004. On the baroclinic structure of the Brazil Current–Intermediate Western Boundary Current system at 22°–23°S, *Geophysical Research Letters* **31**(14): 1–5.

SILVEIRA, I. C. A. D., LIMA, J. A. M., SCHMIDT, A. C. K., CECCOPIERI, W., SARTORI, A., FRANSCISCO, C. P. F. & FONTES, R. F. C. 2008. Is the meander growth in the Brazil Current system off Southeast Brazil due to baroclinic instability?, *Dynamics of Atmospheres and Oceans* **45**(3): 187–207.

SILVEIRA, I. C. A. D., SCHMIDT, A. C. K., CAMPOS, E. J. D., GODOI, S. S. & IKEDA, Y. 2000. A Corrente do Brasil ao largo da costa leste brasileira, *Revista Brasileira de Oceanografia* **48**(2): 171–183. In Portuguese.

SOUTELINO, R., DA SILVEIRA, I., GANGOPADHYAY, A. & MIRANDA, J. 2011. Is the Brazil Current eddy-dominated to the north of 20°S?, *Geophysical Research Letters* **38**(3): 1–5.

STRAMMA, L. & ENGLAND, M. 1999. On the water masses and mean circulation of the South Atlantic Ocean, *Journal of Geophysical Research: Oceans* **104**(C9): 20863–20883.

SZUTS, Z., BLUNDELL, J., CHIDICHIMO, M. & MAROTZKE, J. 2012. A vertical-mode decomposition to investigate low-frequency internal motion across the Atlantic at 26°N, *Ocean Science* **8**(3): 345–367.

URBANO NETO, D. F. & SILVEIRA, I. C. A. D. 2003. Estrutura dinâmica das contracorrentes equatoriais do Oceano Atlântico ao longo de 44°W, *Revista Brasileira de Geofísica* **21**: 145–161.

VALLA, D., PIOLA, A. R., MEINEN, C. S. & CAMPOS, E. 2018. Strong mixing and recirculation in the northwestern Argentine Basin, *Journal of*

Geophysical Research: Oceans **123**(7): 4624–4648.

VISBECK, M. 2002. Deep velocity profiling using lowered acoustic Doppler current profilers: Bottom track and inverse solutions, *Journal of Atmospheric and Oceanic Technology* **19**(5): 794–807.

WUNSCH, C. 1997. The vertical partition of oceanic horizontal kinetic energy, *Journal of Physical Oceanography* **27**(8): 1770–1794.

SUPPLEMENTARY MATERIAL

Considering that the extrapolation scheme used in this work is made by a linear dynamic mode projection of data using a weight scheme, some issues must be considered before applying this technique. There are three main factors that can influence the success of applying this method, which are: (i) the number of modes used in the extrapolation; (ii) the weight values used on the extrapolation; (iii) the depth level to which data are extrapolated. In this supplementary material, we discuss these factors separately and demonstrate their influence on the results. For the sake of brevity, we choose only one LADCP transect, which was the one obtained during the CERESIV cruise. We use this transect as an example, but the following discussion can be generalized to any other cases.

i) Number of Vertical Modes.

Since the extrapolation is based on a Gauss-Markov least squares fit, the number of modes used in this projection affects the final result, and hence impacts the distribution of the amplitudes of each mode on Eq. (4). An increase in the number of modes used to extrapolate the velocity data tends to (but not necessarily will) impact positively the final result since it has the ability to provide a more accurate fit. Another impact generated by the number of modes chosen is related to their inherent vertical profiles, for example, the barotropic mode presents no vertical gradient, the first baroclinic mode crosses the 0 velocity value once, the second baroclinic mode crosses it twice, and so on for further modes. These patterns, when combined, depending upon the number of modes used, may create regions of increasing velocities in depths in which their maximum may coincide or do not cancel each other out. This scenario is displayed on Supplementary Figure S1, especially on the use of 3 modes case (Supplementary Figure S1d), where an intensification happens on the profile farthest from the coast, which can be visualized on Supplementary Figure S2.

ii) Weight matrix values.

As shown in Eq. (6), an important *a priori* assumption is the equipartition of the energy between the two first dynamic modes, with a progressive decreasing of weights for the following modes. Hence, one can argue about the effects of using another weight scheme keeping the equipartition. As expected, changing the weights of each mode contribution on Eq. (6) will change the final result. In Supplementary Figure S3 we have an example comparing the extrapolation for CERESIV cruise using the weight scheme obtained from the independent mooring C3 (W_1, ratio 1/5:1:1/10:1/100:1/100:1/100), a progressive decreasing following Wunsch (1997) (W_2, ratio 1:1:1/2:1/4:1/8:1/16), and an overshooting for the second and third baroclinic modes (W_3, ratio 1/2:1/2:1:1:1/4:1/8). There is an infinite possibility of weights to be used that can also achieve good results, however, in this study we based our analysis on an independent set of time series from current meter moorings, with arguments regarding the mean and first EOF vertical structures.

iii) Reference level of VMADCP acquisition.

Another important topic that can modify the extrapolation performance is the reference level
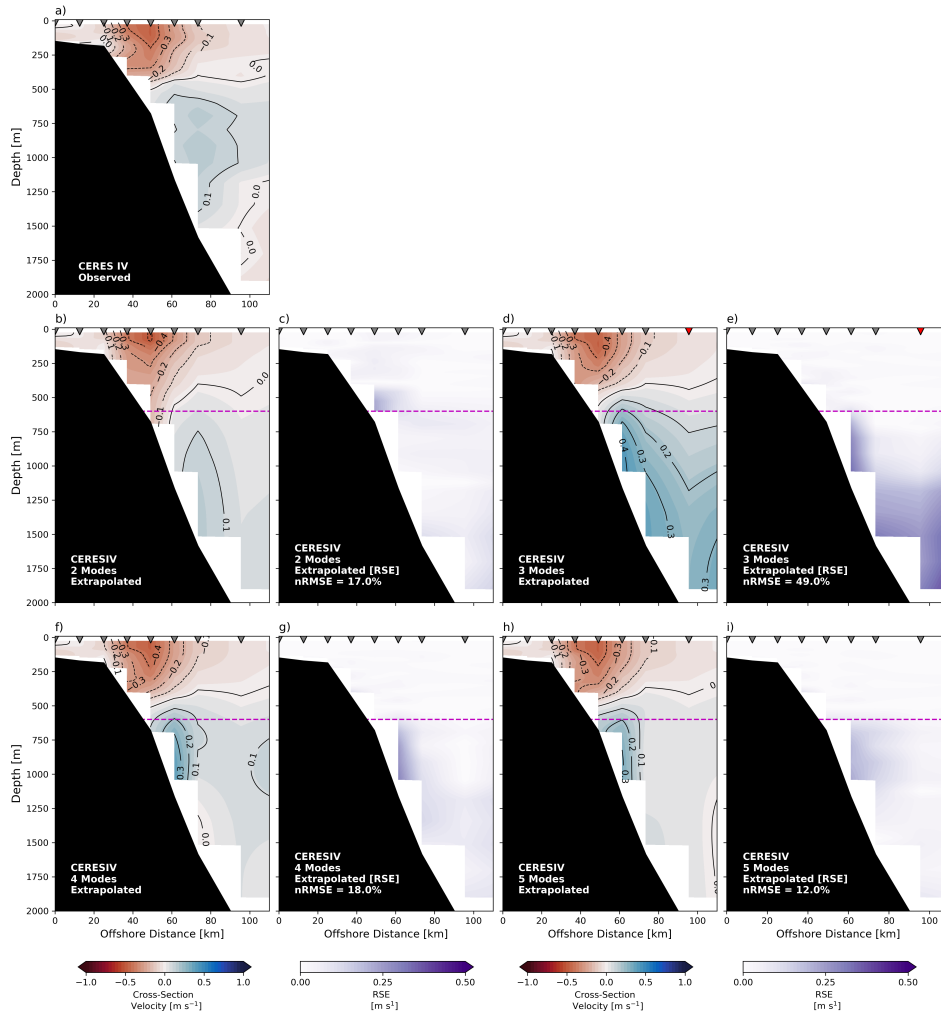
Figure S1. Extrapolated velocity transects for the CERESIV data using different number of vertical modes and their respective root squared error (RSE) in comparison to the observed field. Magenta dashed lines denote the depth in which velocity data was excluded and gray triangles are the CTD stations, red triangles on (d) and (e) highlight the station displaced on Figure S2.

in which data is available, which varies depending on VMADCP instrument frequency. In this study, we choose as reference the depth of 600 m, that mimics a nominal depth in which 75 kHz VMADCP reaches. However, 150 kHz VMADCP usually reaches 300 m, and 38 kHz VMADCP, 1000 m. With increasing (decreasing) this depth level, the number of z points available to perform the dynamic projection also changes directly. It's expected that with an increase in the number of available points, a more robust fit, and consequently, extrapo-

lation is produced, and the opposite is valid for a decrease in the number of points. Supplementary Figure S4 shows a comparison between the adopted 600 m simulating 75 kHz VMADCP acquisition, with 300 m and 1000 m reference levels, simulating 150 kHz and 38 kHz VMADCPs, respectively. Using 300 m as reference level did not reproduce the IWBC (Supplementary Figure S4c), however, using 1000 m produced an IWBC core very similar to the one observed (Supplementary Figures S4d and S4a, respectively). Furthermore, this
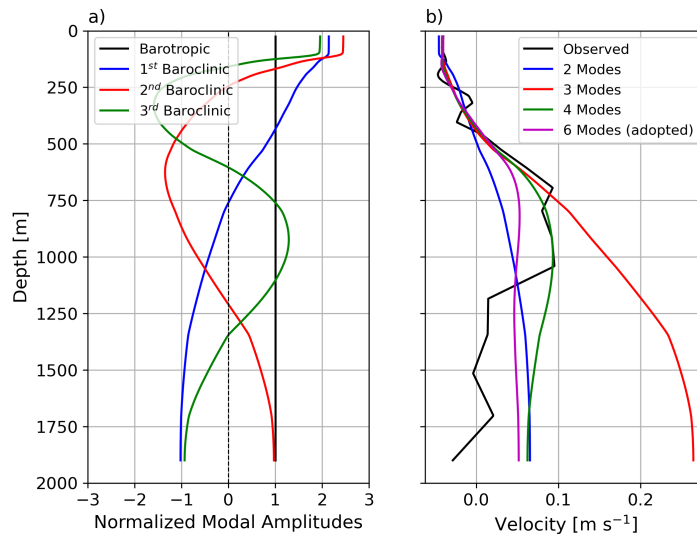
Figure S2. a) The observed 4 first vertical modes derived from CTD profile at the station farthest from the coast for CERESIV transect; b) Reconstructed LADCP velocity profile using a different number of modes at the station farthest from the coast for CERESIV transect.

extrapolation has also the potential to be applied on different acquisition frequencies from VMADCPs.
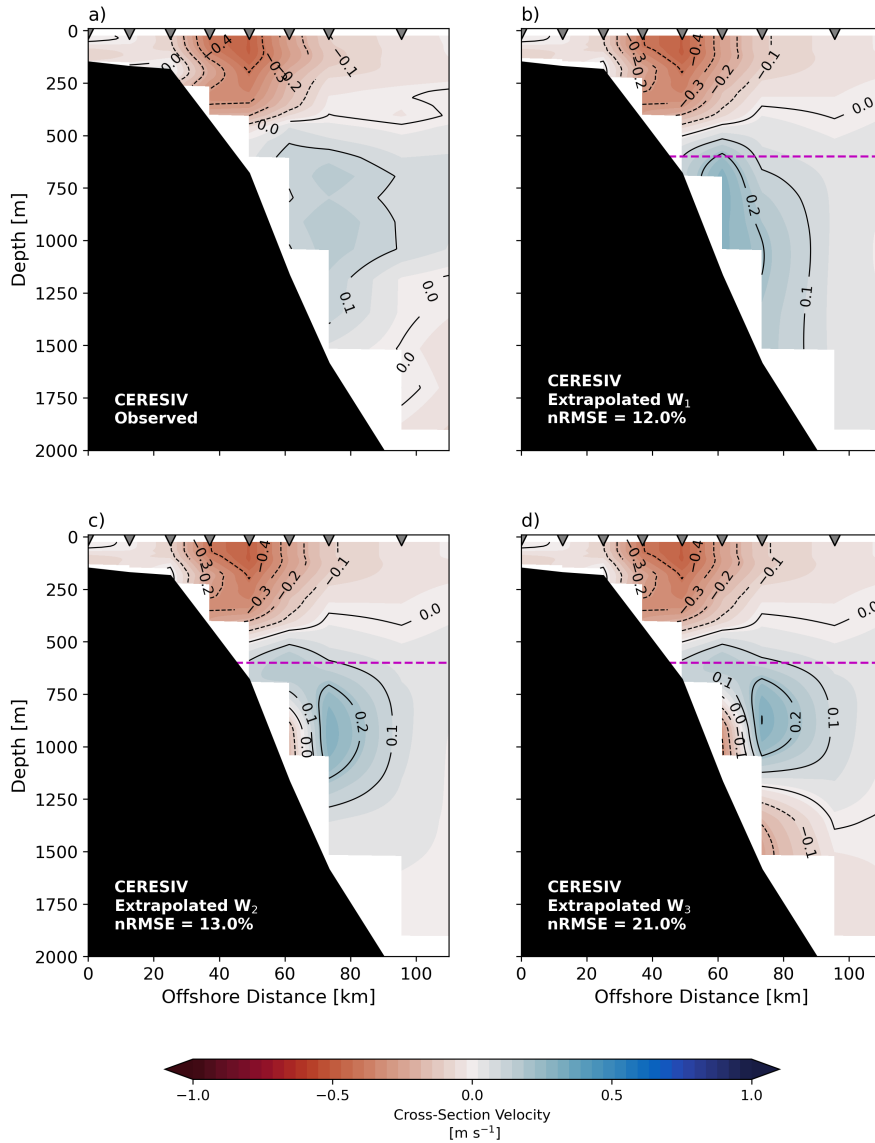
Figure S3. a) Observed velocity transect for the CERESIV cruise; b) Extrapolated velocity transect using the weight scheme W_1; c) the same as (b) but using the weight scheme W_2; d) the same as (d) but using the weight scheme W_3. Magenta dashed lines denote the depth in which velocity data was excluded and gray triangles are the CTD stations.
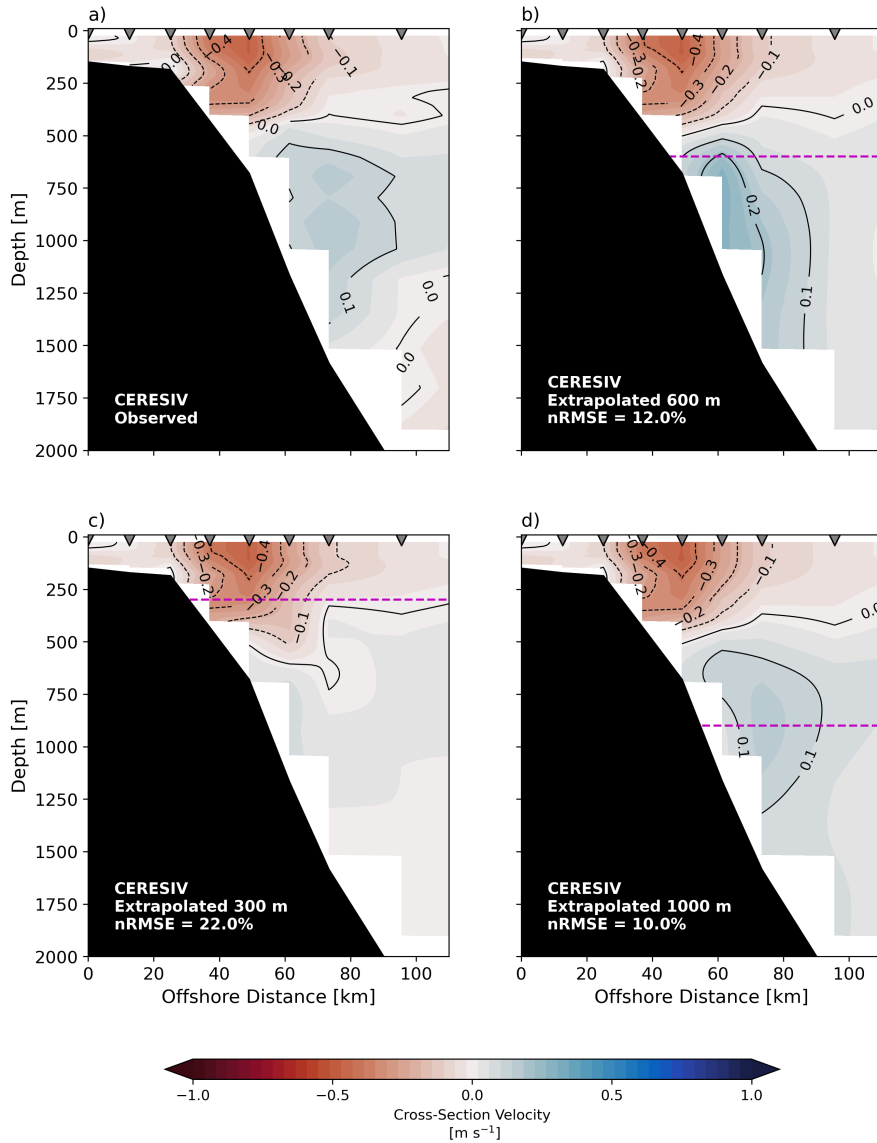
Figure S4. a) Observed velocity transect for the CERESIV cruise; b) Extrapolated velocity transect excluding all data below 600 m c) the same as (b) but excluding all data below 300 m; d) the same as (b) but excluding all data below 900 m. Magenta dashed lines denote the depth in which velocity data was excluded and gray triangles are the CTD stations.